X-ray scattering study of the order parameters in multiferroic TbMnO3

Danny Mannix, D. F. Mcmorrow, A. T. Boothroyd, D. Prabhakaran, Yves Joly, B. Janousova, Claudio Mazzoli, Luigi Paolasini, Stuart B. Wilkins

X-ray scattering study of the order parameters in multiferroic $TbMnO_3$

D. Mannix,[1] D. F. McMorrow,[2,3] R. A. Ewings,[4] A. T. Boothroyd,[4] D. Prabhakaran,[4] Y. Joly,[5] B. Janousova,[6] C. Mazzoli,[6] L. Paolasini,[6] and S. B. Wilkins[6]

[1]*XMaS CRG Beamline, European Synchrotron Radiation Facility, F-38043 Grenoble, France*

[2]*London Centre for Nanotechnology and Department of Physics and Astronomy, University College London, United Kingdom*

[3]*ISIS Facility, Rutherford Appleton Laboratory, Chilton, Didcot OX11 0QX, United Kingdom*

[4]*Department of Physics, Clarendon Laboratory, University of Oxford, Oxford, United Kingdom*

[5]*CNRS-Grenoble, Grenoble, France*

[6]*European Synchrotron Radiation Facility, F-38043 Grenoble, France*

(Received 18 May 2007; revised manuscript received 9 July 2007; published 16 November 2007)

We report on an extensive investigation of the multiferroic compound $TbMnO_3$ using x-ray scattering techniques. Nonresonant x-ray magnetic scattering (NRXMS) was used to characterize the domain population of the single crystal used in our experiments. This revealed that the dominant domain is overwhelmingly *A* type. The temperature dependence of the intensity and wave vector associated with the incommensurate magnetic order was found to be in good agreement with neutron scattering data. X-ray resonant scattering experiments were performed in the vicinity of the Mn *K* and Tb L_3 edges in the high-temperature collinear phase, the intermediate temperature cycloidal and ferroelectric phase, and the low-temperature phase. In the collinear phase, where according to neutron diffraction only the Mn sublattice is ordered, resonant *E*1-*E*1 satellites were found at the Mn *K* edge associated with *A*-type but also *F*-type peaks. Detailed measurements of the azimuthal dependence of the *F*-type satellites (and their absence in the NRXMS experiments) leads us to conclude that they are most likely nonmagnetic in origin. We suggest instead that they may be associated with an induced charge multipole. At the Tb L_3 edge, resonant *A*- and *F*-type satellites were observed in the collinear phase again associated with *E*1-*E*1 events. We attribute these to a polarization of the Tb 5*d* states by the ordering of the Mn sublattice. On cooling into the cycloidal and ferroelectric phase, a new set of resonant satellites appear corresponding to *C*-type order. These appear at the Tb L_3 edge only. In addition to a dominant *E*1-*E*1 component in the σ-π' channel, a weaker component is found in the preedge with σ-σ' polarization and displaced by −7 eV with respect to the *E*1-*E*1 component. Comprehensive calculations of the x-ray scattering cross section were performed using the FDMNES code. These calculations show that the unrotated σ-σ' component of the Tb L_3 *C*-type peaks appearing in the ferroelectric phase contains a contribution from a multipole that is odd with respect to both space and time, known in various contexts as the anapole. Our experiments thus provide tentative evidence for the existence of a type of anapolar order parameter in the rare-earth manganite class of mulitferroic compounds.

DOI: 10.1103/PhysRevB.76.184420 PACS number(s): 75.25.+z

I. INTRODUCTION

Materials possessing more than one "ferroic" order (which includes magnetism, ferroelectricity, elastic distortions, etc.) are referred to as multiferrroic. Although multiferroics are rare—magnetism requiring a partially filled electronic shell, while canonical ferroelectrics such as $BaTiO_3$ have an empty one—they are of considerable interest both from a fundamental point of view and from the possibilities that they offer in the field of spintronics. Recently, the $RMnO_3$ and RMn_2O_5 (R=rare earth) series of compounds have attracted a considerable amount of attention, as it has been shown that members of these series are multiferroic and display novel effects.[1–6] In the case of $TbMnO_3$, for example, a giant magnetoelectric effect has been reported allowing the electric polarization to be switched by applied magnetic fields.[1] Correspondingly, it has been shown in $HoMnO_3$ that the magnetic response can be controlled by an applied electric field.[3] Of key importance in understanding the functionality of these materials is to obtain a complete description of the various order parameters.

To shed further light on the nature of the order parameters in $TbMnO_3$, we have employed x-ray scattering techniques, with an emphasis on exploiting the rich possibilities offered by x-ray resonant scattering (XRS). In an XRS experiment, the photon energy is tuned close to an absorption edge and an excited intermediate state is created by transitions between core and valence shells. At resonance, the scattering amplitude of a single ion can be described by a tensor, whose properties are related directly to specific terms in the multipolar expansions of the electric charge and magnetization.[7] XRS is now well established as being capable of revealing a great diversity of ordering phenomena in solids. These are usually probed via the pure excitation channels *E*1-*E*1 and *E*2-*E*2, where the two distinct channels arise from selection rules for the change in angular momentum ΔL between the core and excited states $\Delta L(E1\text{-}E1) = \pm 1$ and $\Delta L(E2\text{-}E2) = \pm 2$, respectively. For such events, the tensors are even parity and are ranked according to their behavior under time reversal as time odd, for magnetic, and time even for charge orderings. If, however, the ions are located in crystallographic positions which lack a center of inversion symmetry (odd parity), hybridization will occur between the valence orbitals of that atom and transitions may then occur via mixed processes to the hybridized states, giving rise to

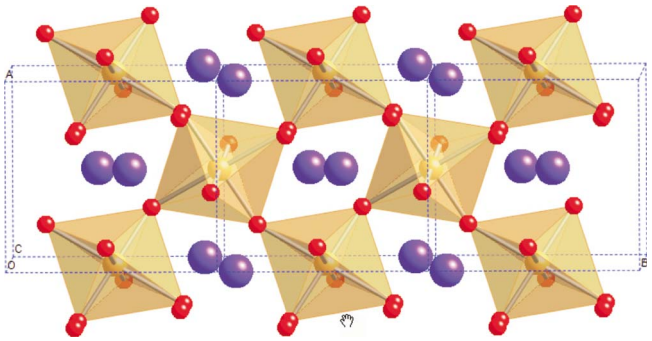

FIG. 1. (Color online) The crystal structure of $TbMnO_3$ in its high-temperature (Pbnm) phase shown in projection down the **c** axis.

parity-odd $E1$-$E2$ events. Such events open up new and interesting possibilities for studying ordering phenomena driven by parity-odd multipoles. For example, magnetoelectric toroidal moments may develop, which can be visualized as arising from placing a series of magnetic dipole moments end to end so as to form a closed circular path.[8] Such moments are characterized as having odd symmetry with respect to parity and can have odd or even symmetry in time reversal. These toroidal moments have historically been referred to as anapoles first considered in the context of multipolar expansions in nuclear physics.[9] Multipoles associated with $E1$-$E2$ processes have been shown to be of importance in nonreciprocal and natural circular dichroism[10–12] and recent predictions having been made for XRS experiments.[13–16]

At room temperature, $TbMnO_3$ adopts an orthorhombic structure, space group *Pbnm*, with lattice parameters $a=5.316$ Å, $b=5.831$ Å, and $c=7.375$ Å (Fig. 1). The Mn and Tb ions occupy the $4b$ (point symmetry $\bar{1}$, i.e., inversion symmetry) and $4c$ (point symmetry m) sites, respectively. Neutron diffraction experiments have shown that the Mn^{3+} magnetic moments order below $T_{N1}=41$ K to form an incommensurate, longitudinally polarized structure (hereafter referred to as the collinear phase) described by a wave vector $(0,q_{\mathrm{Mn}},0)$ with $q_{\mathrm{Mn}}=0.28-0.29\ b^*$.[17,18] In this collinear phase, the Tb moments are thought to be disordered.[17] Below $T_{N2}=28$ K, the magnetic structure becomes noncollinear (hereafter referred to as the cycloidal phase) by developing a component of the magnetization on the Mn sublattice along the **c** axis and, at exactly the same temperature, the material becomes ferroelectric.[17] According to modeling of the neutron diffraction, the Tb moments in this phase order at the same wave vector as the Mn moments but are transversely polarized along the **a** axis. On further cooling below $T_{N3}=7$ K, the Tb moments undergo a further transition and develop a component of the magnetization at a distinct wave vector of $(0,q_{\mathrm{Tb}},0)$ with $q_{\mathrm{Tb}}=0.42\ b^*$, again thought to be transversely polarized along the **a** axis. Kenzelmann *et al.*[17] have argued that the transition to a ferroelectric state results from a loss of a center of inversion symmetry when the magnetic structure changes from being collinear to noncollinear at $T_{N2}=28$ K. This idea has generated considerable interest, and ferroelectric transitions driven by the formation of noncollinear magnetic structures have now been reported in a number of systems.[19,20] Several different theoretical approaches have been developed to explain the magnetoelectric properties of this class of multiferroic,[21,22] which suggest that the macroscopic electric polarization **P** is related to the magnetic moment $\mathbf{S}_i$ by

$$\mathbf{P} = a\mathbf{e}_{ij} \times (\mathbf{S}_i \times \mathbf{S}_j),$$

where e_{ij} is a vector connecting the spins on sites i and j, and a is a constant.

It should be noted that a certain degree of inconsistency exists in the neutron diffraction literature concerning the magnetic structure adopted by $TbMnO_3$. In $TbMnO_3$, the magnetic reflections may be classified into four distinct types, which have been shown to have distinct temperature dependences.[17,18,23,24] The F-type structure gives rise to magnetic reflections classified by $h+k=$even, $l=$even, the G-type reflections with $h+k=$odd, $l=$odd, the C-type with $h+k=$odd, $l=$even, and the A-type structure gives reflections corresponding to $h+k=$even, $l=$odd. In the original investigation by Quezel *et al.*,[25] strong A-type and weak G-type magnetic peaks were reported, with the systematic absence of C-type and F-type reflections. Blasco *et al.*[26] obtained similar results from powder neutron diffraction. In their neutron work on a large single crystal of $TbMnO_3$, Kajimoto *et al.*[18] found evidence for all A-, F-, C-, and G-type structures. The A- and G-type structures have their moments unambiguously along the **b** axis, but attempts to determine the moment directions for the F- and C-type structures could only constrain the direction to be either the **c** or **a** axis. The more recent neutron investigation by Kenzelmann *et al.*[17] reported only the A-type reflections with moments along the **b** axis in the collinear phase, in agreement with Kajimoto *et al.* A plausible explanation for the observation of the different magnetic structures in these experiments is that they depend on details of sample growth and preparation. All neutron investigations, however, agree on one thing: the A-type structure is always the dominant phase. It is also worth noting that the magnetic order is accompanied by weak charge satellites at $2q_{\mathrm{Mn}}$, which have been observed with neutron and nonresonant x-ray scattering.[27,28]

Our experiments on $TbMnO_3$ were undertaken in the spirit of exploring whether the well documented characteristics of XRS could be exploited to reveal information complementary to that provided by neutron diffraction. In particular, the element and electron shell specificity of x-ray resonant magnetic scattering (XRMS) is often used to isolate the contribution from individual components in systems with more than one type of magnetic species, such as $TbMnO_3$. A second major objective of our study was to investigate whether the loss of inversion symmetry that must accompany the transition to the ferroelectric state in $TbMnO_3$ allows new terms in the XRS cross section to become visible, such as $E1$-$E2$ terms associated with the ordering of parity-odd multipoles.[13–16]

This paper is organized as follows. In the next section, we outline the experimental details, including a description of the scattering geometries (crystal orientation, x-ray polarization, definition of azimuth, etc.) employed in our experiments. In Sec. III, we present the experimental results, which

for clarity of exposition is further subdivided into subsections. Our attempts to characterize the magnetic domain structure of our sample using NRXMS are described in Sec. III A. The results of the XRS investigations in the collinear phase at the Mn K edge are described in Sec. III B, while in Sec. III C, we describe the outcome of XRS experiments in the collinear phase at the Tb L_3 edge. XRS investigations undertaken in the cycloid phase, again at the Mn K and Tb L_3 edges, are described in Secs. III D and III E, respectively. Results taken in the the low-temperature regime, $T<8$ K, at the Tb L_3 edge are presented in Sec. III F. The investigation of the $2q$ charge satellites is presented in Sec. III G. Our results are analyzed and discussed in Sec. IV, in the light of calculations of the electronic structure using the FDMNES code.[29] In the final section, we summarize our work.

II. EXPERIMENTAL DETAILS

Single crystals of $TbMnO_3$ were prepared in Oxford by the floating zone method in an image furnace. The crystals were cut and polished to produce samples with either the **b** or **a** axis as the surface normal. The samples were investigated by superconducting quantum interference device magnetometery and were found to display the same behavior as previously reported.[30] The lattice parameters refined in our synchrotron experiments were in very good agreement with those deduced from neutron scattering results and the our crystal mosaic was found to be $\approx 0.03°$. These observations indicate that the samples used in our studies were of excellent quality with comparable bulk magnetic properties to other samples described in the literature.

The scattering experiments were undertaken at the XMaS and ID20[31] magnetic scattering beamlines at the ESRF, Grenoble, France. XMaS views radiation from a bending magnet and employs a vertical scattering geometry (σ-polarized incident photons). The sample used on XMaS was cut and polished with **b** axis as the surface normal (see Fig. 2 for the definition of photon polarizations and coordinate system used in our experiment). The experiments on the undulator beamline ID20 were performed also mainly with the same vertical geometry as on XMaS. Some additional experiments on ID20 were carried out in a normal beam geometry, with the scattering plane approximately horizontal, corresponding to π-polarized incident photons. XRS measurements were undertaken around the Mn K (6.552 keV) and Tb L_3 (7.515 keV) edges, using a Cu(220) or Au(222) polarization analyser, respectively. The wave-vector resolution was of the same order of magnitude in all our x-ray experiments, typically $\approx 1\times 10^{-4}$ (rlu) reciprocal lattice units. The photon flux on ID20 is approximately 1×10^{13}/s in a focused spot size of about 0.3×0.4 mm^2 (vertical $\times$horizontal); on XMaS, the corresponding numbers are 5×10^{11}/s in 0.8×0.5 mm^2 at an x-ray energy of 8 keV and 200 mA current in the ESRF storage ring. The intense photon flux on ID20 carries with it the potential to heat the sample. Checks were made for such an effect, and when present (typically for sample temperatures below 10 K), the incident beam was attenuated by up to an order of magnitude. A key aspect of our experiments has been the utilization of the high flux from the ID20 undulator source, which enabled us to perform NRXMS to characterize the magnetic domains present in the near surface volume probed by the x rays. These experiments were undertaken with incident energy of 7.470 keV using a Au(222) polarization analyzer.

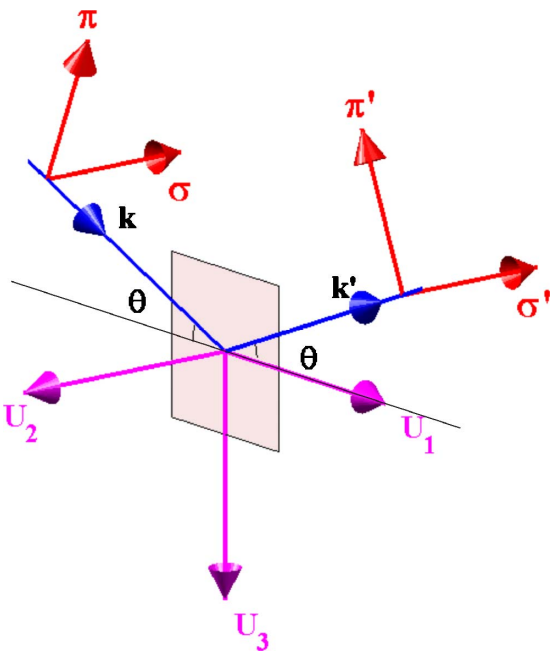

FIG. 2. (Color online) Definitions of the nomenclature used to label the polarization state of the photon beam and the coordinate system used to resolve the components of the magnetic moments relative to the incident and scattered beams.

In the following, we use the conventional notation to describe the polarization conditions of the incident and scattered photon beams, σ-σ' and π-π' for incident polarization scattered without rotation and σ-π' and π-σ' for photons scattered with a 90° rotation of their electric vector.

In our experiments, extensive use was made of scans of the azimuthal angle ψ, i.e., rotation around the scattering vector.[32] In recent years, the azimuthal dependence of XRS has been exploited increasingly in studies of systems displaying magnetic and multipolar order. The reason is that the variation of the resonant intensity in a scan of the azimuthal angle reflects directly the symmetry of the intermediate states (orbitals) through which the resonance proceeds. By way of example, we show in Fig. 3(a) the azimuthal dependence of the space-group forbidden (3,0,0) reflection recorded at the Tb L_3 edge on XMaS. The intensity displays a $\cos^2\psi$ dependence in agreement with calculations of $E1$-$E1$ Templeton scattering[33,34] for the *Pbnm* space group. In both the experiments on samples with **b** or **a** faces as the surface normal direction, the crystal was oriented with the **c** axis in the scattering plane, which defined the $\psi=0$ of the azimuthal scans. Due to the construction of the diffractometers used in our experiments, azimuthal scans could only be performed in the vertical scattering geometry, and then mainly for reflections parallel to the **b** axis.

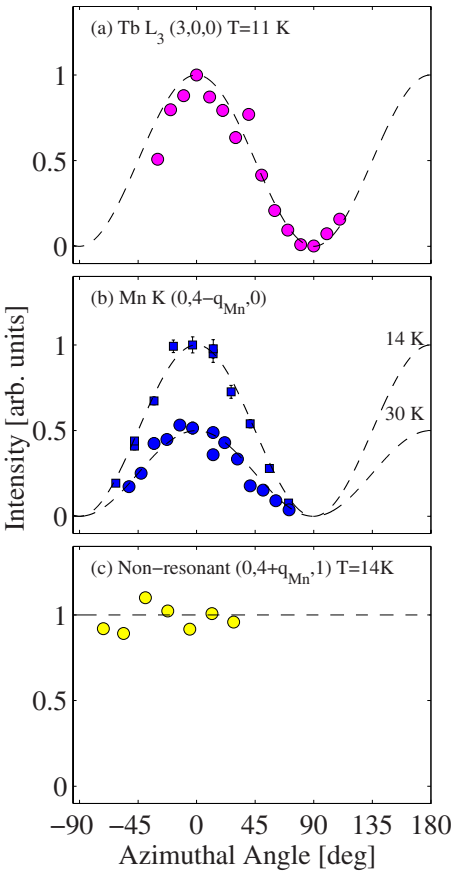

FIG. 3. (Color online) Summary of azimuthal scans of various diffraction peaks recorded at different temperatures and photon energies. The data were recorded in the σ-π' channel and have been normalized to unity. The lines are guides to the eyes.

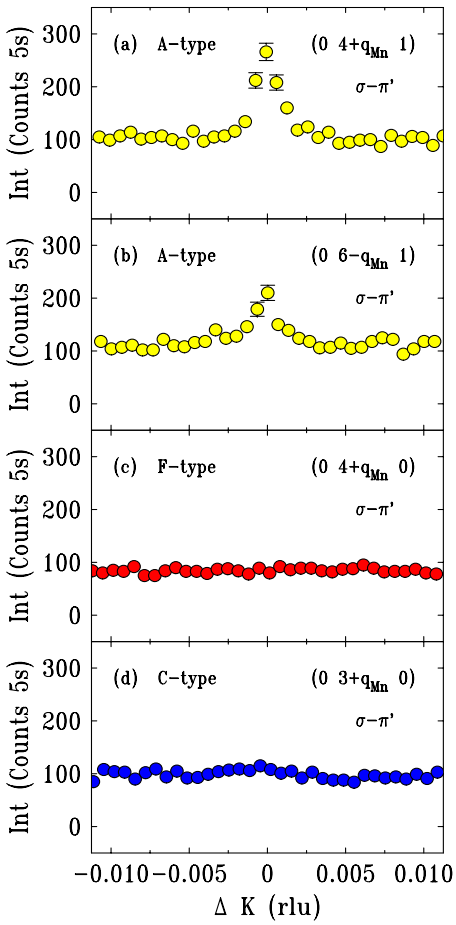

FIG. 4. (Color online) Summary of the nonresonant x-ray magnetic scattering observed on ID20 in scans of wave-vector transfer parallel to $\mathbf{b}^*$ through various positions in reciprocal space associated with the *A*-, *F*-, or *C*-type magnetic structures. The data were recorded in the ferroelectric and cycloidal phase at $T=14$ K, at an azimuth of $\psi=0$, and in the σ-π' channel.

III. EXPERIMENTAL RESULTS

A. Magnetic structure investigation with nonresonant x-ray magnetic scattering

In order to ascertain which magnetic domains were present in our sample and, in particular, to understand any effects that may arise in the near surface region probed in our x-ray measurements, we initially investigated the NRXMS. Time constraints and the weakness of the signal prevented us from making exhaustive studies in the NRXMS regime. Nevertheless, these investigations turned out to be helpful in the interpretation of our XRS results.

The NRXMS experiments were undertaken at a temperature of $T=14$ K, where all the possible *A*-, *F*-, *C*-, and *G*-type reflections were found to be present in the study of Kajimoto *et al.*[35] The crystal was oriented initially at an azimuth of $\psi=0$, and a photon energy of 7.470 keV was selected, below the Tb L_3 edge. The scattered intensity calculated for NRXMS can be written as[36]

$$I^{\sigma\text{-}\sigma'} = V_d(S_2 \sin 2\theta)^2,$$

$$I^{\sigma\text{-}\pi'} = V_d\{(-2\sin^2\theta)[(\cos\theta)(L_1+S_1) - S_3\sin\theta]\}^2, \quad (1)$$

where L_1, S_1, S_2, and S_3 are the components of orbital and spin moments along orthogonal axes U_1, U_2, and U_3 (Fig. 2), θ is the scattering Bragg angle, and V_d represents the domain volumes of the $d=A$-, *F*-, *C*-, or *G*-type structures within the illuminated sample volume. Upon azimuthal rotation, consideration should be given in Eq. (1) for the change in the magnetization components along the U_1, U_2, and U_3 axes, so that, for example, $S_2(\psi)=S_2(\psi=0)\cos\psi - S_1(\psi=0)\sin\psi$.

The results of our NRXMS investigations are summarized in Figs. 4 and 5 for the σ-π'- and σ-σ'-polarized intensities, respectively. From Eq. (1), it can be seen that the σ-π' channel is sensitive to magnetic moments in the scattering plane along U_1 and U_3, and the σ-σ' channel is sensitive to magnetic moments directed perpendicular to the scattering plane along U_2. In Fig. 4, significant NRXMS intensity is evident for wave vectors corresponding to the *A*-type magnetic structure, $(0,4\pm q,1)$ and $(0,6\pm q,1)$. [The slightly weaker intensities found at $(0,6\pm q,1)$ compared to $(0,4\pm q,1)$ is probably due to the decreasing magnetic form factor rather than the geometric terms in Eq. (1).] Scans, taken at wave vectors corresponding to the *F*-type and *C*-type structures, at $(0,4\pm q,0)$ and $(0,3\pm q,0)$ are shown in Figs. 4(c) and 4(d), where no peaks are visible above the background. Turning to

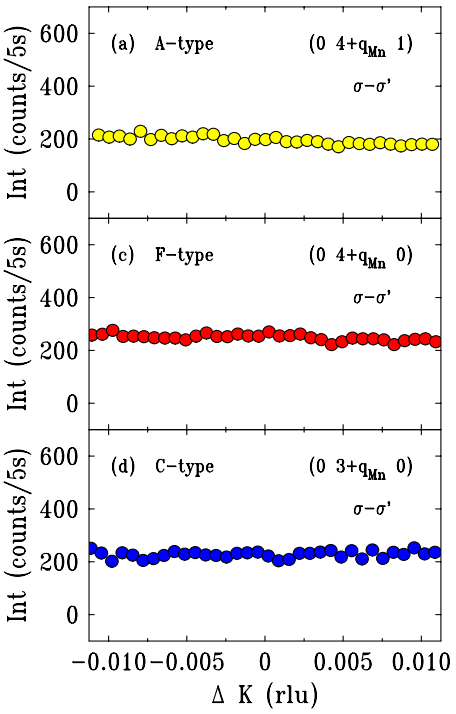

FIG. 5. (Color online) Summary of the nonresonant x-ray magnetic scattering observed on ID20 in scans of wave-vector transfer parallel to $\mathbf{b}^*$ through various positions in reciprocal space associated with the *A*-, *F*-, or *C*-type magnetic structures. The data were recorded in the ferroelectric and cycloidal phase at $T=14$ K, at an azimuth of $\psi=0$, and in the σ-σ' channel.

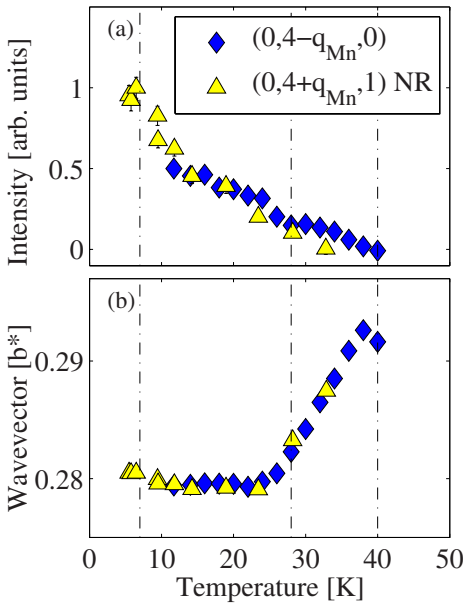

FIG. 6. (Color online) Temperature dependence of the intensity and modulation wave vector of various satellites. In (a) and (b), we compare the Mn *K* edge and nonresonant data, all recorded in σ-π'. For ease of comparison, the intensities have been normalized to unity at low temperature. The data were taken at ID20.

the σ-σ' channel, summarized in Fig. 5, we found no evidence for NRXMS for the wave vectors investigated, indicating that the magnetic moments in this phase are confined to the **b**-**c** plane.

Thus, the fact that we observe satellite reflections in our NRXMS experiments at positions $(h,k\pm q,l)$, with $h+k$ even, l even, appears to indicate that our sample is predominantly *A* type. Due to the fact that we do not observe any peaks in the unrotated σ-σ' channel leads us to conclude that in our sample, and at a temperature well inside the cycloidal phase, the magnetic moments are in the **b**-**c** plane. In this way, our sample appears to share a similar domain configuration to the one studied by Kenzelmann *et al.* who found that in this phase, the moments form a cycloid in the **b**-**c** plane. Further information on the orientation of magnetic moments in our sample was provided by studying the azimuthal dependence of the $(0,4\pm q,1)$ satellite, shown in Fig. 3(c). The intensity depends only weakly on azimuth, which from Eq. (1), implies that the moments have their strongest component along the **b** direction. It should be noted that the weak azimuth dependence observed could also arise from two magnetic domains oriented along both the **a** and **c** axes in our scattering geometry. However, the absence of magnetic scattering in the σ-σ' channel is not consistent with such a scenario.

The temperature dependence of the intensity of NRXMS observed at $(0,4\pm q,1)$ is shown in Fig. 6(a), where it appears to agree with that deduced from neutron scattering experiments, increasing steadily below $T_{N1}=41$ K. We also find good agreement with neutron scattering for the thermal evolution of the magnetic wave vector, as shown in Fig. 6(b), starting at a value of about 0.29 at T_{N1}, decreasing in value as the sample is cooled through the collinear phase, before appearing to lock into a value of about 0.28 below T_{N2} in the ferroelectric phase. However, in agreement with the neutron data, it is clear that this is not a genuine lock-in transition, as below T_{N2} the value of the wave vector increases slightly down to the base temperature.

The conclusion to be drawn from our NRXMS investigation is that the dominant magnetic structure in our sample appears to be *A* type, with the magnetic moment oriented mainly along the **b** axis. No evidence is found for the *F*-type or *C*-type structures, presumably because either they are not present or their domain volumes are too small to allow them to be observed.

B. Collinear phase: Mn *K* edge

Turning to our XRS studies, we first investigated the response with incident energy tuned close to the maximum of the Mn fluorescence spectrum [Fig. 7(a)] and with the sample cooled into the collinear phase ($T_{N2}\leqslant T\leqslant T_{N1}$). Under these conditions, scans in reciprocal space were performed to search for the existence of satellite peaks. Well defined diffraction satellites were found [Figs. 8(c) and 8(d)] at nominal *A*-type magnetic wave vectors such as $(0,k\pm q,1)$, with $q\approx 0.285\ b^*$, close to the value of q_{Mn} deduced from neutron diffraction experiments. An additional set of satellites was discovered at *F*-type positions, $(0,k\pm q,0)$ k even [Figs. 8(a) and 8(b)]. Both sets of satel-

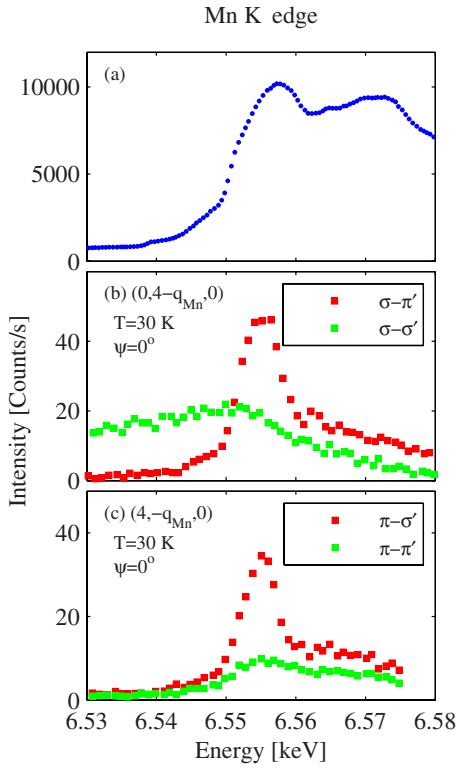

FIG. 7. (Color online) (a) Fluorescence spectrum in the vicinity of the Mn K edge. [(b) and (c)] Representative energy dependence of the x-ray resonant scattering near the Mn K edge at various satellite positions and for various polarization geometries. The data were taken at ID20.

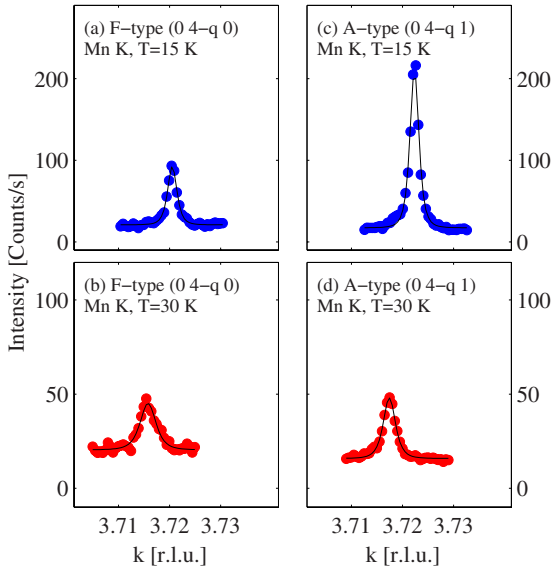

FIG. 8. (Color online) Representative scans of the wave-vector transfer with the photon energy tuned to the peak of the resonance at the Mn K edge. The scans shown are through the positions of F-type [(a) and (b)] and A-type [(c) and (d)] reflections and were recorded in the σ-π' channel at ID20.

lites were found in the rotated σ-π' channel only. Extensive searches at C-type positions such as $(0,3\pm q,0)$ failed to find any evidence for XRS at the Mn K edge in this phase. The observation of both A- and F-type reflections at the Mn K edge is difficult to reconcile with the NRXMS presented in Sec. III A, where peaks attributable to the A-type structure only were present. Moreover, the data in Fig. 8 also show a similar intensity at the A- and F-type reflections in the collinear phase. This would appear to undermine any claim that the latter is magnetic scattering from a minority F-type phase: neutron scattering studies always show that A type is dominant. We comment on possible explanations for the discrepancy between the NRXMS and XRS later.

In Fig. 7(b), we show the energy dependence of the $(0,4-q,0)$ at 30 K for incident σ and the $(4,-q,0)$ for π-polarized photons [Fig. 7(c)], as the photon energy is tuned through the Mn K edge. The resonant response is seen to exhibit a maximum at an energy of 6.557 keV, slightly above the position of the first derivative in the absorption at 6.552 keV. The energy of the resonance allows us to identify unambiguously the maximum with $E1$-$E1$ dipole transitions, which at the Mn K edge probe the $4p$ states. (A weak, preedge feature at 6.540 keV is also evident.) The scattering was found to be mostly in the rotated channel. The scattering in the unrotated channel is more difficult to interpret with any certainty, due to changes in the diffuse charge scattering and the onset of fluorescence at the edge.

To further address the nature of the order revealed by the F-type peaks, the azimuthal dependence of the scattering of the $(0,4-q,0)$ at the Mn K edge was determined with the results shown in Fig. 3(b) for the σ-π' channel. The scattering is seen to display the same $\cos^2\psi$ dependence as the (3,0,0) space-group forbidden reflection [Fig. 3(a)]. The $E1$-$E1$ XRMS amplitude can be expressed as[37]

$$A_{res}^{mag} = \begin{pmatrix} \sigma\text{-}\sigma' & \pi\text{-}\sigma' \\ \sigma\text{-}\pi' & \pi\text{-}\pi' \end{pmatrix} = \begin{pmatrix} 0 & \hat{z}_1 \cos\theta + \hat{z}_3 \sin\theta \\ \hat{z}_3 \sin\theta - \hat{z}_1 \cos\theta & -\hat{z}_2 \sin 2\theta \end{pmatrix}. \quad (2)$$

Here, the amplitude is written as a matrix in a basis of the linear components of the polarization perpendicular (σ) and parallel (π) to the scattering plane, for the incident (unprimed) and scattered (primed) beams, and $\hat{\mathbf{z}}$ is a unit vector parallel to the magnetic moment, with Cartesian components defined with respect to the orthogonal axes U_1, U_2, and U_3 (Fig. 2). The above equation establishes that $E1$-$E1$ XRMS is forbidden in the σ-σ' channel and is sensitive to the magnetic moments in the scattering plane for the σ-π' channel. Thus, the twofold azimuthal symmetry we observe at $(0,4-q,0)$ [Fig. 3(b)], with the maximum at $\psi=0$, could be consistent with magnetic scattering from an F-type structure for which the magnetic moments would have to be orientated along the **c** axis. This moment direction is in agreement with that deduced from neutron scattering experiments.[18] However, when we compare our expectations for the NRXMS response that would arise from such an F-type structure, with moments oriented along the **c** axis, we fail to find consistency with our own NRXMS results for the

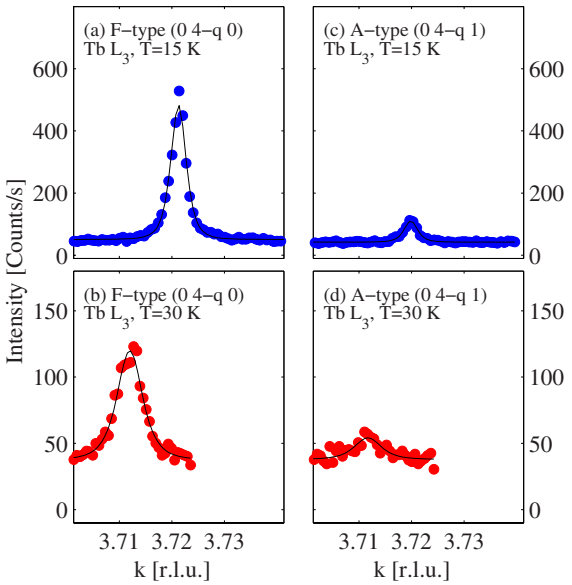

FIG. 9. (Color online) Representative scans of the wave-vector transfer with the photon energy tuned to the peak of the resonance at the Tb L_3 edge. The scans shown are through the positions of F-type [(a) and (b)] and A-type [(c) and (d)] reflections and were recorded in the σ-π' channel at ID20.

absence of signal at $(0,4+q,0)$. From Eq. (2), using the Bragg angles at the Mn K edge $\theta(0,4-q,0)=40$ and $(0,4-q,1)=29.7$, the measured XRMS intensity ratio $I[(0,4+q,1)]/I[(0,4+q,0)]$ can be used to obtain the expected volume ratio V_A/V_F for the F-type and A-type structures. This leads to the ratio $V_A/V_F=3$. We can then plug this ratio into Eq. (1) for the nonresonant scattering described in Sec. III A, using the NRXMS Bragg angles $(0,4-q,0)=34.8$ and $(0,4-q,1)=23.8$, and calculate the NRXMS intensity we would expect at $(0,4+q,0)$. However, from this, we find that the NRXMS should be significantly larger than that observed at $(0,4+q,1)$, not zero as we have found.

Further doubt that the XRS at $(0,4\pm q,0)$ is magnetic in origin comes from its temperature dependence. The thermal evolution of the $(0,4-q,0)$ σ-π' intensities are shown in Fig. 6(a) and appear to follow closely the A-type $(0,4-q,1)$ magnetic intensities that we measured using NRXMS. The close agreement in the temperature dependence is in contrast to that revealed in neutron diffraction experiments.[18] In these measurements, the temperature dependence for the two structures is very different: the F-type intensities increase at a slow rate below $T_{N1}=41$ K and then increase dramatically below $T_{N3}=7$ K due to the apparent stabilization of the F-, G-, and C-type structures by the onset of the Tb magnetic order.

Also compared in Fig. 6(b) is the temperature dependence of the modulation wave vector at $(0,4-q,0)$ with the nonresonant scattering at $(0,4-q,1)$. Of significance, especially in the light of evidence that the XRS observed at $(0,4-q,0)$ may not be magnetic in origin, is the similar thermal evolution of wave vector to that found for the A-type magnetic scattering we measured at $(0,4-q,1)$ with NRXMS. This effect may suggest that the underlying order parameter

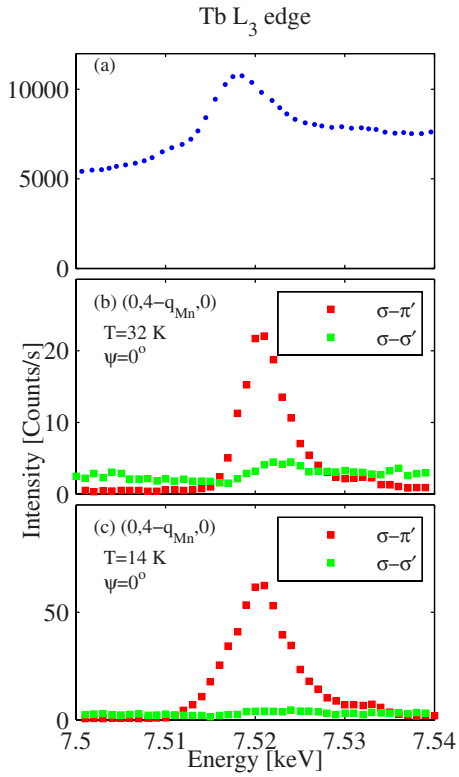

FIG. 10. (Color online) (a) Fluorescence spectrum in the vicinity of the Tb L_3 edges. [(b) and (c)] Representative energy dependence of the x-ray resonant scattering near the Tb L_3 edges at various satellite positions and for various polarization geometries. The data were taken on XMaS.

is driven by the onset of magnetism of the Mn ions, suggesting an interesting coupling of magnetic and charge order parameters in this material.

In summary, in the collinear phase at the Mn K edge, we find A-type reflections at $(0,4-q,1)$, which was the dominant peak in the NRXMS study. Its dependence on energy, polarization, temperature, etc., have the hallmarks of an XRMS process, where the ordering of the local Mn $3d$ moments leads to a polarization of the $4p$ band. The peak at the F-type position $(0,4\pm q,0)$ is less easy to interpret. If it is attributed to also being an XRMS peak, then we can infer that for the F-type structure, the Mn moments are polarized along the **c** axis. However, the characteristics of the $(0,4\pm q,0)$—not least of which is its absence in our NRXMS study—force us to consider other possible origins for this peak. If this order parameter is not a magnetic order and given that it can be associated with $E1$-$E1$ events, we may suppose that the XRS arises from $E1$-$E1$ time-even events associated with a charge multipole. Moreover, given that its wave vector follows so closely with the magnetic order, this order parameter would have to be coupled linearly to the magnetism of the Mn sublattice.

C. Collinear phase: Tb L_3 edge

Experiments were also performed in the collinear phase for photon energies in the vicinity of the Tb L_3 edge. Reso-

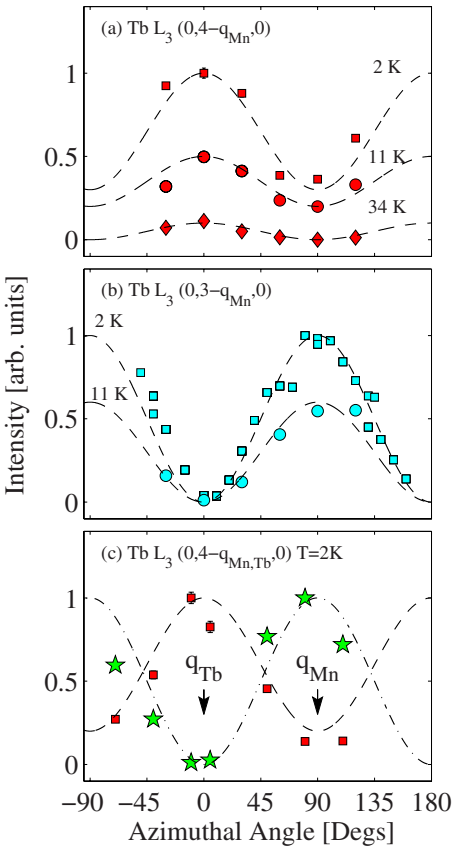

FIG. 11. (Color online) Summary of azimuthal scans of various diffraction peaks recorded at different temperatures and photon energies. The data were recorded in the σ-π' channel and have been normalized to unity. The lines are guides to the eyes. The azimuth ψ=0 corresponds to the **c** axis in the scattering plane.

nant satellites were found at positions corresponding to both the nominal Mn A-type magnetic satellites at $(0,4\pm q,1)$ and the seemingly anomalous peaks at $(0,4\pm q,0)$. Representative scans of the wave-vector transfer parallel to $\mathbf{b}^*$ are shown in Fig. 9, where sharp diffraction peaks are evident reflecting the long-range nature of the ordering probed. Polarization analysis of these showed that the scattering was predominantly in the rotated σ-π' channels. The observation of these satellites is particularly notable as, according to all previous neutron scattering studies, the Tb moments in the collinear phase are disordered. The data in Figs. 9(a) and 9(b) also appear to show that far from being the weaker peaks, at the Tb L_3 edge, the F-type peaks are actually considerably more intense than the A-type peaks. Such comparisons should, however, be qualified by the fact that at the Tb L_3 edge, a marked asymmetry in the intensity of the $\pm q$ satellites was present [see Fig. 17(b)].

The energy dependence of $(0,4\pm q,0)$ is shown in Fig. 10(b). Inspection of the energy scans allows us to ascribe the resonances to $E1$-$E1$ processes, which in the case of the Tb L_3 edge connect $2p$ to $5d$ states. The azimuthal dependence of the $(0,4\pm q,0)$ σ-π' intensities is shown in Fig. 11(a) and can be seen to exhibit the same $\cos^2\psi$ dependence, as found at the Mn K edge [Fig. 3(b)]. The temperature dependence of the $(0,4\pm q,0)$ intensities and wave vectors are shown in Fig. 12, where we find that they follow exactly the temperature dependence of the XRS observed at the Mn K edge.

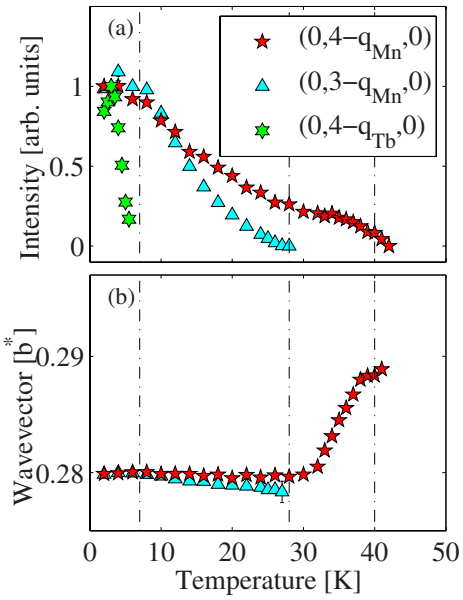

FIG. 12. (Color online) Temperature dependence of the intensity and modulation wave vector at the Tb L_3 edge recorded in σ-π'. For ease of comparison, the intensities have been normalized to unity at low temperature.

From these observations, we can immediately deduce that in the interval $T_{N2} \leqslant T \leqslant T_{N1}$, in other words well above any ordering of the Tb^{3+} dipole moments, the $5d$ states at the Tb sites are polarized by ordering of the Mn magnetic moments and with a modulation wave vector identical to that of the Mn sublattice. (In this context, we note that induced polarizations have been reported on the anion species of several actinide materials.[38]) This of course does not answer the question of the nature of the polarization that is created at the Tb sites and hence the origin of the scattering process which gives rise to the resonances. We consider the various possibilities in Sec. IV.

D. Ferroelectric and/or cycloidal phase: Mn *K* edge

It is of considerable interest to follow the XRS at the Mn K edge on entering the ferroelectric phase. In the model proposed by Kenzelmann *et al.*, ferroelectricity arises when the Mn sublattice makes the transition from a collinear to noncollinear structure, removing the inversion center at the Mn site. In principle, the loss of inversion symmetry may be detected directly in XRS experiments as the opening of new $E1$-$E2$ scattering channels in the region of the preedge.[13–16]

The most complete data set that we have on changes to the XRS spectra at the Mn K edge on entering the ferroelectric phase was taken with incident π-polarized photons. The temperature dependence of the resonant line shape of the F-type satellite $(4,-q,0)$ is summarized in Fig. 13. In the collinear phase at 30 K, the scattering is predominantly in the rotated π-σ' channel, with a smooth, weaker response in the unrotated channel, most likely associated with the onset

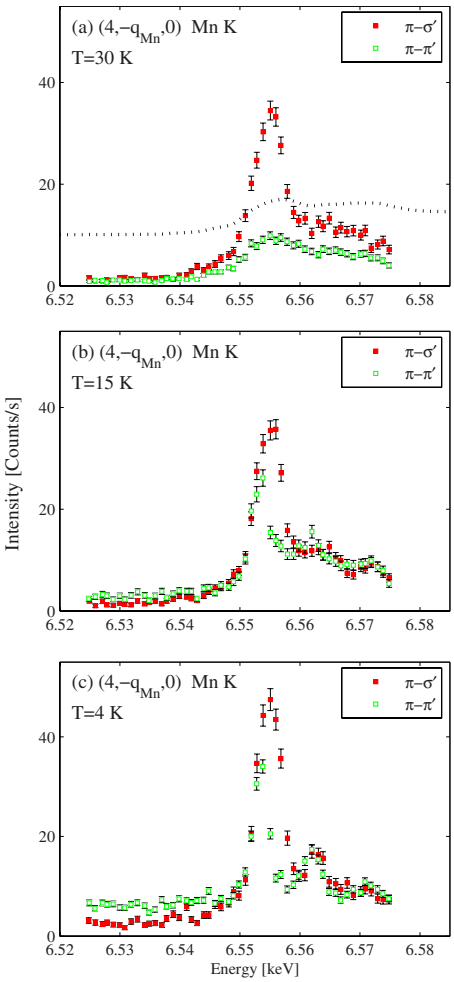

FIG. 13. (Color online) Energy dependence of XRS at the $(4, -q_{\mathrm{Mn}}, 0)$ satellite in the vicinity of the Mn K edge collected using a normal beam geometry with π incident photons on ID20.

of fluorescence at the edge. On cooling into the ferroelectric phase, a dramatic change occurs in the unrotated channel with a peak appearing displaced to lower energy by 2 eV from the peak in the response in the rotated channel. With further cooling, the intensity of the unrotated component increases until it becomes comparable in magnitude to the rotated one. In addition, a feature appears above the edge in both channels.

Inspection of Eq. (2) reveals that for π-polarized incident photons, $E1$-$E1$ XRMS scattering from a longitudinally modulated magnetic structure polarized along **b** should occur in the π-π' channel only. This is exactly the opposite of what is shown in Fig. 13(a), where the predominant scattering occurs in the π-σ' channel. Further consideration of Eq. (2) indicates that if the peak is to be ascribed to XRMS, then the moments in the collinear phase are instead polarized along **a** or **c**. Consistency with the data on the $(0,4\pm q,0)$ satellites (Sec. III B) can be achieved when we recall that azimuthal scans at this peak position suggested moments polarized along **c**. The appearance of significant intensity in the unrotated channel on entering the ferroelectric phase [Fig. 13(b)] might then further be explained, for an $E1$-$E1$ XRMS process, by the development of a component of the magnetization along the **b** axis. However, this interpretation would seem to be untenable as the intensity in the unrotated channel peaks 2 eV below that in the rotated one, indicating that the former is not pure $E1$-$E1$. Here, the caveats raised in Secs. III B and III C about interpreting the F-type peaks as XRMS should also be recalled. We do not observe any C-type XRS peaks at positions such as $(0,3\pm q,0)$ at the Mn K edge, which indicates that these Mn magnetic domains are absent in our sample, in agreement with our NRXMS results.

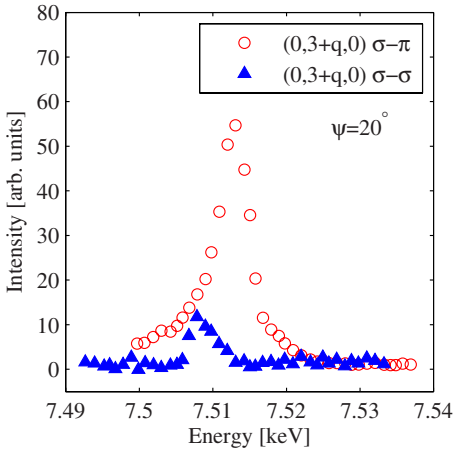

FIG. 14. (Color online) Energy dependence of XRS at the $(0,3-q_{\mathrm{Mn}},0)$ satellite in the vicinity of the Tb L_3 edge recorded on ID20. The data were taken at a temperature of $T=14$ K, and the azimuth was set to be $\psi=20°$, i.e., close to the minimum in the intensity of the response in the σ-π' channel [Fig. 11(b)].

E. Ferroelectric and/or cycloidal phase: Tb L_3 edge

Upon cooling into the cycloidal phase $T_{N2} \leqslant T \leqslant T_{N1}$, a new set of C-type resonant satellites at $(0,k\pm q,0)$ k odd were revealed at the Tb L_3 edge. These were found to be absent at the same temperature at the Mn K edge and unlike the A-type and F-type reflections, we do not find any charge order satellites at $2q_{\mathrm{Mn}}$ associated with these C-type peaks. Key data on their energy dependence measured at $(0,3+q,0)$ are shown in Fig. 14, where it is apparent that the intensity appears mostly in the rotated σ-π' channel. The azimuthal dependence of the $(0,3+q,0)$ is shown in Figs. 11(b) and 20, where it is seen to have a $\sin^2\psi$ dependence, in antiphase to the azimuthal dependence found at $(0,4+q,0)$ shown in Figs. 3(b) and 11(a). At these C-type reflections, energy scans also reveal a weaker preedge feature, as seen in Fig. 14, which is scattered with the σ-σ' polarization. The azimuthal dependence in this channel has a $\cos^2\psi$ azimuthal dependence.

The temperature dependence of the σ-π'-polarized intensities is shown in Fig. 12(a), where they are seen to disappear above $T_{N2}=28$ K. Magnetic satellites were also identified at these wave vectors in the neutron scattering investigation by Kenzelmann *et al.*[17] and were attributed to an induced moment on the Tb ions, oriented along the **a** axis, from the onset of the Mn magnetic structure in the cycloid phase.

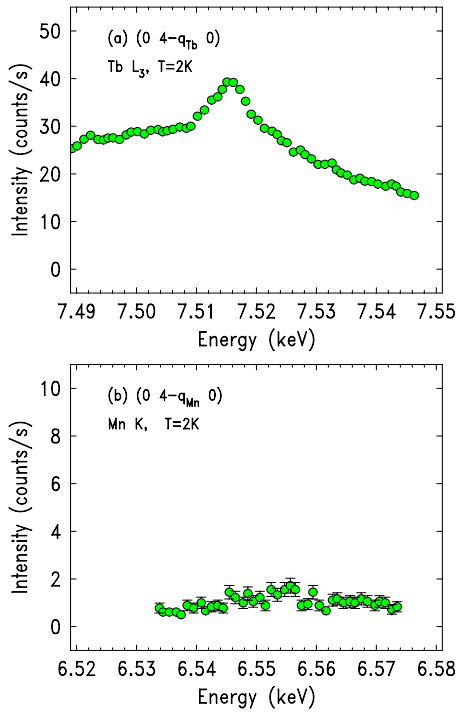

FIG. 15. (Color online) (a) Energy scan taken at the Tb ordering wave vector $q_{\mathrm{Tb}}=0.42$ at $T=2$ K in the σ-π' channel, where only a weak XRS is observed. (b) Energy scan taken at the Mn ordering wave vector $q_{\mathrm{Mn}}=0.28$ at $T=2$ K, where no significant XRS is observed.

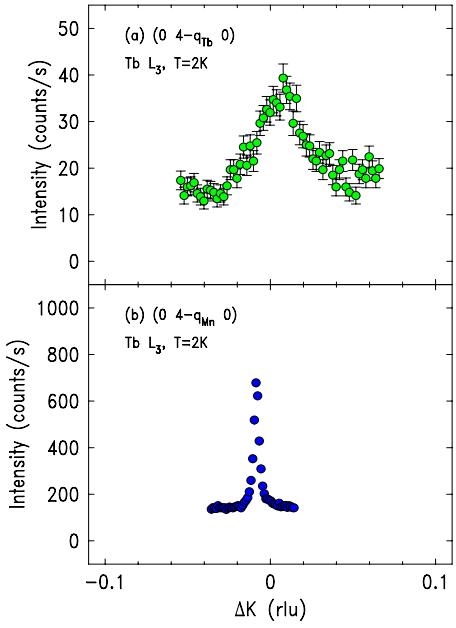

FIG. 16. (Color online) (a) k scan taken at the Tb ordering wave vector $q_{\mathrm{Tb}}=0.42$ at $T=2$ K in the σ-π' channel. The broad width of the scattering indicates that the underlying magnetic order is only short ranged ordered at this temperature. (b) k scan taken at the Mn ordering wave vector $q_{\mathrm{Mn}}=0.28$ at $T=2$ K, indicating that the induced polarization on the Tb ions is long ranged ordered at this position.

From Eq. (2), it can be seen that the observed azimuthal dependence is consistent with a magnetic moment directed along the **a** axis. Detailed analysis described in Sec. IV substantiates this further but also indicates that the weak preedge feature in the unrotated channel shown in Fig. 14 may reflect the contribution from an order parameter with both odd time and inversion symmetries.

In summary, in the cycloidal phase, additional XRS satellites appear at $(0,k\pm q,0)$, k odd, for photon energies around the Tb L_3 edge, but not the Mn K edge. They are found predominantly in the rotated polarization channel and are most probably $E1$-$E1$ XRMS from a polarization of the Tb $5d$ states along the **a** axis induced by the onset of the Mn cycloidal order. These findings are in agreement with the model of Kenzelmann *et al.* for this phase.

It is of course important to reconcile these XRS observations at the Tb edge with our failure to observe NRXMS at $(0,k\pm q,0)$, k odd, discussed in Sec. III A. This may be achieved if we suppose that the Tb $4f$ moments are only weakly polarized in the cycloidal phase. This combined with the higher background [Fig. 5(d)] observed in the σ-σ' channel where the peak would be expected to occur [Eq. (1)] would then act to render the peak unobservable.

F. Low-temperature phase: Tb *L* edge

We have additionally investigated the XRS below $T_{N3}=7$ K, where the Tb moments order, with the distinct wave vector of $(0,q_{\mathrm{Tb}},0)$ with $q_{\mathrm{Tb}}=0.42$ b^*. However, in this phase, energy scans taken at q_{Tb} find only a weak XRS response, as shown in Fig. 15(a). The peak in the energy scan at the Tb L_3 edge is close to the maximum of the fluorescence spectrum and allows us to associate the XRS as arising from $E1$-$E1$ transitions, probing the Tb $5d$ states. For completeness, we also show in Fig. 15(b) an energy scan of q_{Tb} taken at the Mn K edge, where no significant XRS can be identified. This implies that, within the accuracy of our measurements, we find no evidence for an induced polarization of the Mn ions from the onset of the Tb order.

A scan of the wave-vector transfer parallel to $[0k0]$ through q_{Tb} provides us with more information about the weakness of the XRS, Fig. 16(a). This scan reveals that the peaks associated with q_{Tb} are very broad in reciprocal space, even at the lowest temperature measured (2 K) and are therefore consistent with only short-range order. Presumably, this effect arises from the competition of magnetic order at this position with the induced Tb ordering we identify at $(0,k\pm q,0)$, k odd. Indeed, it is intriguing that these XRS investigations appear to find that the major polarization of the Tb valence electrons arises from the Mn $3d$ order and not from the ordering of the Tb $4f$ ions. The short ranged order at q_{Tb} has also been reported in forgoing neutron investigations.[17,26] It may be of significance that the coupling of Mn and Tb moments have been invoked as higher order terms in the nearest-neighbor and next-nearest-neighbor model to explain the emergence of the incommensurate spin structure in the heavy rare-earth $ReMnO_3$ systems.[18,30]

The azimuthal dependence of the $(0,4-q_{\mathrm{Tb}},0)$ is shown in Fig. 11(c) and has an identical azimuthal symmetry as

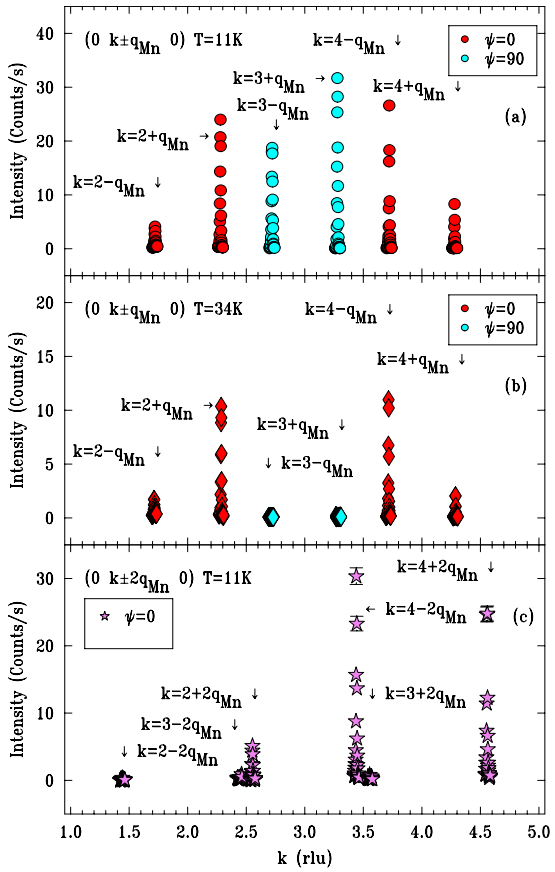

FIG. 17. (Color online) Summary of scans of the wave-vector transfer along $[0,k,0]$ [(a) and (b)] XRS data around the primary satellite positions $(0,k\pm q_{\mathrm{Mn}},0)$ at the Tb L_3 edge for azimuthal angles of $\psi=0$ and 90° in the σ-π' channel. (c) Nonresonant, charge satellites at $(0,k\pm 2q_{\mathrm{Mn}},0)$ in the σ-σ' channel.

those recorded at $(0,k\pm q,0)$, k odd, as shown in Fig. 11(b). This comparison indicates that the low-temperature ordered Tb magnetic moments are oriented along the **a** axis. The temperature dependence of the intensity of the $(0,4-q_{\mathrm{Tb}},0)$ is shown in Fig. 12(a), where it disappears above T_{N3} in agreement with neutron scattering results.

G. Charge satellites

We have also investigated the satellites which occur at $2q_{\mathrm{Mn}}$ in $TbMnO_3$. We found that these satellites around a given A-type magnetic wave vector such as $(0,4-q,1)$ do not resonate at either the Tb or Mn absorption edges. Of significance is the fact that we also found $2q_{\mathrm{Mn}}$ satellites associated with $(0,4-q,0)$. This result suggest that the charge degrees of freedom also couple to the lattice causing the charge order satellites that we observed and indicating an intricate interplay of magnetic and charge lattice coupling in this material. We also found that these $2q_{\mathrm{Mn}}$ peaks do not resonate at either absorption edge. Key data on the wave-vector scans are shown in Fig. 17 for the resonant q_{Mn} and nonresonant $2q_{\mathrm{Mn}}$ satellites. It is also noteworthy that we do not find any evidence for charge ordered satellites associated with the C-type satellites such as $(0,3-q,0)$.

IV. ANALYSIS AND DISCUSSION

To obtain a deeper understanding of our resonant scattering investigations, we have performed *ab initio* electronic structure calculations using the FDMNES code,[29] which allowed us to evaluate the XRS spectra, including possible contributions from $E1$-$E1$, $E1$-$E2$, and $E2$-$E2$ processes.

It is important to point out that $E1$-$E1$ XRS can, in most cases, be easily identified because the energy maximum occurs very close to that in the fluorescence spectrum. However, XRS features which occur at energies corresponding to the preedge threshold may arise from $E1$-$E1$, $E2$-$E2$, and $E1$-$E2$ events and cannot be simply interpreted from their position in energy.

A. FDMNES code

FDMNES is a software package that allows the calculation of the intensity of the diffracted reflections in the vicinity of absorption edges of the elements present in the material of interest. The code may use various methods to calculate the excited states probed during the resonant process and, in our calculations, we employed the multiple scattering theory. The final states are calculated in a fully relativistic way, including the spin-orbit contribution. Then, the matrix elements governing the transition process between the initial and final states are calculated considering the polarization conditions of the incoming and outgoing photons. This photon electric field is expanded in order to calculate both the electric dipole ($E1$) and electric quadrupole ($E2$) contributions and consequently for the resonant process, the $E1$-$E1$, $E1$-$E2$, and $E2$-$E2$ components. At the end, the structure factors are calculated and an expansion in a spherical basis is performed, so at the various diffraction satellites, the different contributions coming from all the order of scattering can be separately provided. In this way, one obtains the monopole (F^0), dipole (F^1), and quadrupole (F^2) $E1$-$E1$ contributions, the time-even (+) and time-odd (−) dipoles ($F^1\pm$), quadrupole ($F^2\pm$) and octupole ($F^3\pm$) $E1$-$E2$ contributions, and the monopole, dipole, quadrupole, octupole, and hexadecapole $E2$-$E2$ contributions. For the $E1$-$E2$ component, the nonmagnetic and magnetic parts can be given separately, so it is possible to precisely deduce which terms, in particular, contribute to the XRS intensity.

In practice, one has to provide to the code of the crystallographic structure and a guess of the electronic structure, including the spin polarization. From this, the Dirac equation is solved. At low temperature, neutron diffraction experiments have shown that the crystallographic structure does not change very much[26] from the high-temperature *Pbnm* structure. The main problem in the context of the present study is that even minute changes in crystal structure greatly affect the XRS. We chose to keep the *Pbnm* structure. We built a supercell, four times bigger along the **b** direction to mimic the magnetic modulated structure of Kenzelmann *et al.* In this way, the corresponding new diffraction vectors

TABLE I. The results of FDMNES calculations of XRS multipole intensities at the Mn K edge, in units of r_0^2, in the collinear phase. All calculations were undertaken for azimuth $\psi=0$. The $E1$-$E2$ multipoles are negligible in the calculations because the Mn ions are located at sites with inversion symmetry in the *Pbnm* space group. The even order $E1$-$E1$ and $E2$-$E2$ and the time-even $E1$-$E2$ terms are explicitly zero because they cannot arise from our magnetic structure. In the table, zero means, that the calculated intensities were less than 1×10^{-6}, i.e., very small, not zero.

Collinear phase Mn K edge							
Transition	Multipole	$(0,4\pm q,1)$ $\sigma\sigma'$	$(0,4\pm q,1)$ $\sigma\pi'$	$(0,4\pm q,0)$ $\sigma\sigma'$	$(0,4\pm q,0)$ $\sigma\pi'$	$(0,3\pm q,0)$ $\sigma\sigma'$	$(0,3\pm q,0)$ $\sigma\pi'$
$E1$-$E1$	F^1	0	6×10^{-4}	0	6×10^{-5}	0	0
$E2$-$E2$	F^0	0	0	0	0	0	0
	F^1	0	0	0	0	0	0
	F^3	0	0	0	0	0	0

$(h,k\pm q,l)$ with $q=0.25\ b^*$ is not far from the incommensurate one measured. In order to model the data in the cycloidal phase below T_{N2}, we kept the same diffraction vector with $q=0.25\ b^*$ and allowed the magnetic moment to modulate in the **b**-**c** plane, as described by Kenzelmann *et al.*[17] Making these approximations, we used FDMNES to calculate the XRS intensities at the wave vectors corresponding to A-type $(0,4\pm q,1)$, F-type $(0,4\pm q,0)$, and C-type $(0,3\pm q,0)$ orders, which were extensively investigated in our experiments. In all of the following discussion, intensities below a threshold of $1\times10^{-6}r_0^2$ were taken to be zero. This is a reasonable approximation as from the FDMNES calculations, the intensity at $(0,4\pm q,1)$ at the Mn K edge is $5\times10^{-4}r_0^2$. The corresponding intensity measured in our experiments at ID20 at this wave vector was about 100 counts/s, so that intensities of the order 500 times below this are beyond the sensitivity of our measurements. For the collinear phase, the calculated intensities of all possible multipolar contributions were found to be negligibly small at the Tb L_3 edge, while the results for the Mn K edge in this phase are given in Table I. Corresponding calculated intensities for the cycloidal phase are given in Tables II and III. The $E1$-$E1$ intensities are given 10 eV above the Fermi level (0 eV), while the $E1$-$E2$ and $E2$-$E2$ intensities are given at a preedge value taken 5 eV below the Fermi level.

B. Collinear phase

We first consider our results for the collinear phase, $T_{N2}<T<T_{N1}$. Here, our XRS data reveals two sets of satellites: A type, such as $(0,k\pm q,1)$, and F type $(0,k\pm q,0)$, both with k even. These two sets of satellites showed a resonant behavior at both the Mn K and the Tb L_3 edges. The results of the FDMNES calculation at the Mn K edge, using the **b**-axis-modulated magnetic structure of Kenzelmann *et al.*[17] and the *Pbnm* structure, are shown in Figs. 18(a)–18(c) for the A-type, F-type, and C-type structures, respectively, while the decomposition of the intensity into its multipolar components is given in Table I. The calculations predict finite $E1$-$E1$ F^1 at the A-type wave vectors, of the order $5\times10^{-4}r_0^2$, and that the $E2$-$E2$ intensities are negligibly small. The preedge peaks shown in Fig. 18(a) are all $E1$-$E1$ in origin. The $E1$-$E2$ multipoles are negligible in these calculations since the Mn ions occupy sites with inversion symmetry in the *Pbnm* structure. Interestingly, the code also predicts some finite $E1$-$E1$ XRMS arising from the F^1 multipole at the F-type $(0,4\pm q,0)$ wave vector, which is an order of magnitude weaker than that calculated at $(0,4\pm q,1)$. This result is in contradiction with our x-ray experiments, where we find similar XRS intensities for the A- and F-type peaks at the Mn K edge, as shown in Figs. 8(b) and 8(d), but adds weight to the idea idea that the XRS observed at the F-type

TABLE II. The results of FDMNES calculations of XRS multipole intensities at the Mn K edge, in units of r_0^2, in the cycloidal phase. All calculations were undertaken for azimuth $\psi=0$. The $E1$-$E2$ multipoles are negligible in the calculations because the Mn ions are located at sites with inversion symmetry in the *Pbnm* space group. The even order $E1$-$E1$ and $E2$-$E2$ and the time-even $E1$-$E2$ terms are explicitly zero because they cannot arise from our magnetic structure. In the table, zero means that the calculated intensities were less than 1×10^{-6}, i.e., very small, not zero.

Cycloidal phase Mn K edge							
Transition	Multipole	$(0,4\pm q,1)$ $\sigma\sigma'$	$(0,4\pm q,1)$ $\sigma\pi'$	$(0,4\pm q,0)$ $\sigma\sigma'$	$(0,4\pm q,0)$ $\sigma\pi'$	$(0,3\pm q,0)$ $\sigma\sigma'$	$(0,3\pm q,0)$ $\sigma\pi'$
$E1$-$E1$	F^1	0	1×10^{-3}	0	3×10^{-5}	0	1×10^{-5}
$E2$-$E2$	F^1	2×10^{-6}	2×10^{-6}	2×10^{-6}	2×10^{-6}	2×10^{-6}	2×10^{-6}
	F^3	2×10^{-6}	2×10^{-6}	2×10^{-6}	2×10^{-6}	2×10^{-6}	2×10^{-6}

TABLE III. The results of FDMNES calculations of all XRS multipole intensities at the Tb L_3 edge, in units of e^2, in the cycloidal phase. The $\pm$ for the $E1$-$E2$ multipoles refer to time-even and time-odd multipoles, respectively. All calculations were undertaken for azimuth $\psi=0$, except the $(0,3\pm q,0)$ $\sigma\pi'$ which was calculated at azimuth $\psi=90°$. The even order $E1$-$E1$ and $E2$-$E2$ and the time-even $E1$-$E2$ terms are explicitly zero because they cannot arise from our magnetic structure. In the table, zero means that the calculated intensities were less than 1×10^{-6}, i.e., very small, not zero.

Cycloidal phase Tb L_3 edge							
Transition	Multipole	$(0,4\pm q,1)$ $\sigma\sigma'$	$(0,4\pm q,1)$ $\sigma\pi'$	$(0,4\pm q,0)$ $\sigma\sigma'$	$(0,4\pm q,0)$ $\sigma\pi'$	$(0,3\pm q,0)$ $\sigma\sigma'$	$(0,3\pm q,0)$ $\sigma\pi'$
$E1$-$E1$	F^1	0	5×10^{-3}	0	1×10^{-3}	1.4×10^{-5}	3.9×10^{-4}
$E2$-$E2$	F^1	0	0	0	1.4×10^{-6}	0	0
	F^3	0	0	0	0	0	0
$E1$-$E2$	F^{1-}	0	0	0	3×10^{-6}	5×10^{-5}	0
	F^{2-}	0	0	0	0	4×10^{-6}	0
	F^{3-}	0	0	0	0	6×10^{-6}	0

peaks is not predominantly magnetic in origin. Shifting the Mn ions from their nominal positions in the calculations had the effect of causing larger scattering at the F-type wave vector but yielded azimuthal dependences inconsistent with our experimental data. The FDMNES calculations predict no significant XRS at the C-type peaks, as shown in Fig. 18(c), in agreement with our experimental observations in the collinear phase.

Calculations using FDMNES of the XRS in the collinear phase at Tb L_3 edge were also performed. The calculated XRS spectra are shown in Figs. 19(a)–19(c), where they are seen to be negligibly small in the sense described above.

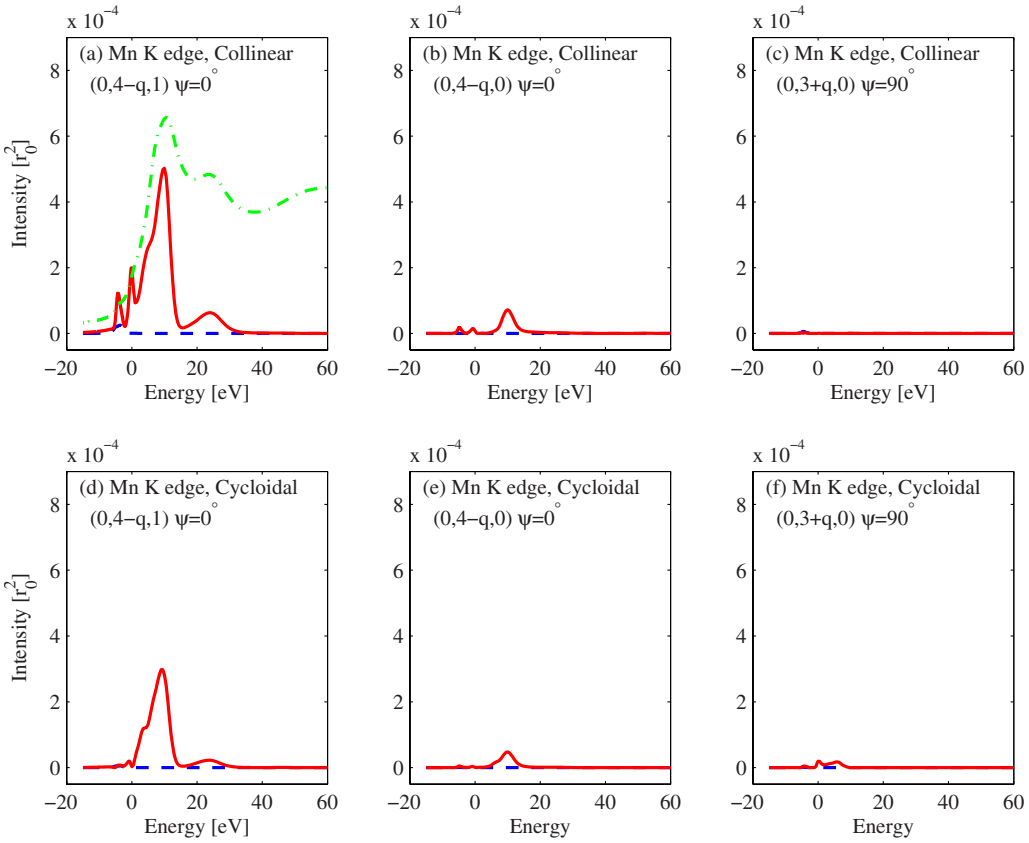

FIG. 18. (Color online) Representative results of FDMNES calculations for $TbMnO_3$ in the vicinity of the Mn K edge for the [(a)–(c)] collinear and [(d)–(f)] cycloidal phases. The calculated x-ray absorption near edge structure (XANES) is given by the dot-dashed line in (a). The figure allows for a comparison of the calculated intensities of [(a) and (d)] A type, [(b) and (e)] F-type, and [(c) and (f)] C-type studied in our experiments. The σ-π' and σ-σ' channels are represented by the solid red and dashed blue lines, respectively.

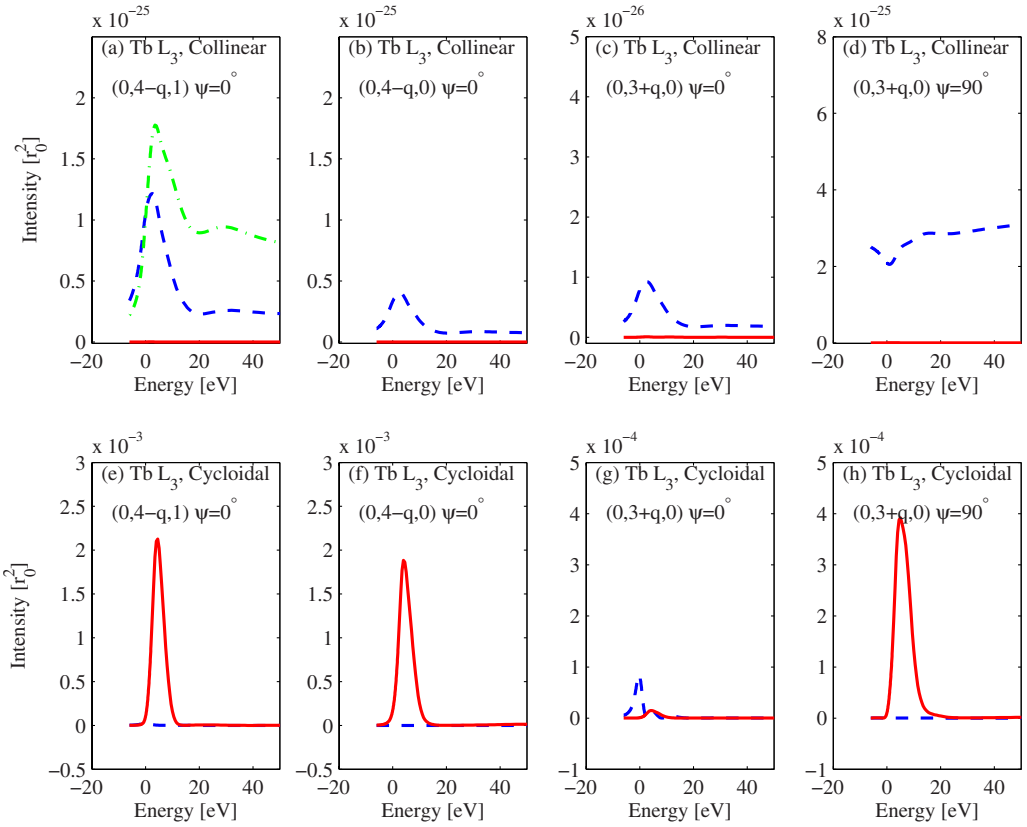

FIG. 19. (Color online) Representative results of FDMNES calculations for $TbMnO_3$ in the vicinity of the Tb L_3 edge for the [(a)–(d)] collinear and [(e)–(h)] cycloidal phases. The calculated XANES is given by the dot-dashed line in (a). The figure allows for a comparison of the calculated intensities of [(a) and (e)] *A* type, [(b) and (f)] *F* type, and [(c), (d), (g), and (h)] *C* type studied in our experiments. The σ-π' and σ-σ' channels are represented by the solid red and dashed blue lines, respectively.

Thus, the calculations do not reproduce our experimental results, where we observed significant XRS intensities at both the *A*- and *F*-type peaks in the collinear phase at the Tb L_3 edge. A possible explanation for this discrepancy is that the FDMNES calculations do not predict a magnetic polarization on the Tb 5*d* states induced from the Mn collinear magnetic structure. However, it is noteworthy that the calculations do identify a polarization on the Tb ions in the cycloid phase (discussed below) for the *C*-type reflections, induced by the Mn cycloid magnetic structure. This induced polarization is in agreement with our experimental results and the neutron scattering results of Kenzelmann *et al.* In the light of this fact, another plausible scenario is that the XRS observed at the Tb edge for both the *A*- and *F*-type peaks is not predominantly magnetic in origin. Instead, they might arise from a charge multipole order parameter, which does not appear with measurable intensity in the calculations because of assumptions made in the model, such as the restriction to the *Pbnm* space group. Neither experiment nor calculations yet provide a conclusive answer to this issue.

C. Cycloidal phase

For the cycloidal phase at the Mn *K* edge, the calculated XRS spectra are shown in Figs. 18(d)–18(f) and the corresponding multipole intensities are summarized in Table II. These calculations predict significant XRMS intensity ($1 \times 10^{-3} r_0^2$) for the *A*-type peak and weaker intensities for the *F*-type ($5 \times 10^{-5} r_0^2$) and *C*-type ($1 \times 10^{-6} r_0^2$) peaks, all of which are magnetic dipole in origin, $E1$-$E1$ F^1. As with the comparison in the collinear phase, there is considerable disagreement between the experiment and calculation in the ratio of intensities at the *A*- and *F*-type peaks. Although the calculations indicate that the *F*-type intensities are around 2 orders of magnitude smaller, our experiments find similar XRS intensities for the two peaks. Again, this may be an indication that the XRS we observed at the *F*-type peaks is not magnetic in origin. The calculations predict a very weak XRS at the *C*-type wave vectors, in disagreement with our experimental results where these peaks were found to be absent. However, this weak intensity may be at the limit of our experimental sensitivity. Again, as in the collinear phase at the Mn *K* edge, all $E1$-$E2$ XRS is calculated to be negligibly small at this absorption edge because the Mn ions are assumed to occupy positions of center inversion symmetry in the *Pbmn* space group.

For the ferroelectric phase, $T_{N3} < T < T_{N2}$, the most striking feature of our XRS data is the appearance of *C*-type, $(0, k \pm q, 0)$, k odd, satellites for photon energies around the Tb L_3 edge. In this phase, the XRS cross section at the Tb L_3 was calculated by inputing the cycloidal magnetic structure. Here, the FDMNES code predicts a measurable scattering intensity due an $E1$-$E1$ XRMS process in the σ-π' channel of 4×10^{-4}. Remarkably, the approximately $\sin^2 \psi$ azimuthal

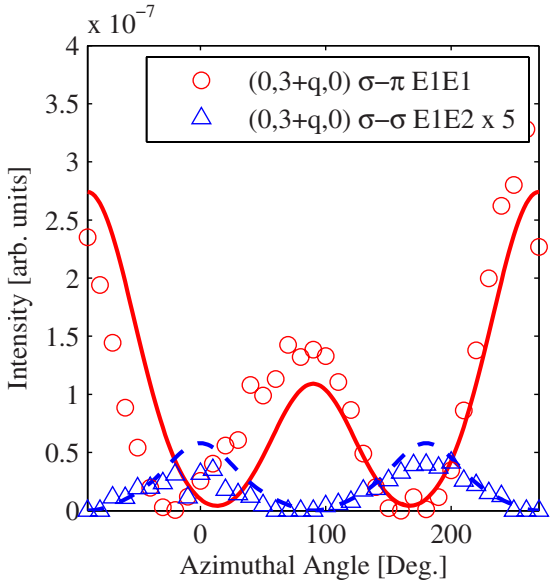

FIG. 20. (Color online) Azimuthal dependence of XRS at the $(0,3-q_{\mathrm{Mn}},0)$ satellite in the vicinity of the Tb L_3 edge recorded on ID20. The σ-π data were taken at an energy corresponding to an $E1$-$E1$ event around 7.520 keV, while the σ-σ data were taken 7 eV below this energy. The lines have been calculated using the FDMNES package. In the unrotated channel, the main contribution is calculated to be from $E1$-$E1$ XRMS associated with a splitting of the Tb $5d$ bands induced by the cycloidal order on the Mn sublattice. For the unrotated channel, the weak preedge peak is calculated to be $E1$-$E2$, arising from an anapole, i.e., a multipole which is odd with respect to both time and parity. The data in the unrotated channel have been multiplied by a factor of 5.

dependence predicted in this channel appears to account for the data shown in Fig. 11(b). The FDMNES code actually reveals that scattering at this wave vector in the rotated channel arises from a small magnetic net polarization of the Tb $5d$ bands along the **a** axis induced by the onset of cycloidal magnetic order on the Mn sublattice. In contrast, only weak XRS intensities were calculated at corresponding wave vectors at the Mn K edge.

The azimuthal symmetry at $(0,k\pm q,0)$, k odd, is actually more complex than the simple $\sin^2\psi$ form suggested by the data in Fig. 11(b) for the σ-π' channel. A much more extensive set of measurements was performed with the results shown in Fig. 20. Not only is the azimuthal dependence clearly more complex, with onefold rather than twofold symmetry, but in addition these experiments revealed the existence of a weak component to the scattering in the unrotated (σ-σ') channel. Most importantly, this component has an azimuthal dependence that peaks in antiphase with the rotated (σ-π') component (Fig. 20) and resonates 7 eV below the position of the $E1$-$E1$ dipole resonance (Fig. 14). The latter fact indicates that it arises either from an $E2$-$E2$ or from an $E1$-$E2$ process. Calculations using the FDMNES code indicate that, although the $E2$-$E2$ and $E1$-$E2$ spectra have similar azimuthal dependences, the σ-σ' signal actually arises mostly from an $E1$-$E2$ event at this position (Table II). Specifically, this component is consistent with the existence of a finite F^{1-} term, a time-odd, parity-odd multipole, which is also known as the anapole. The calculations indicate that the $E2$-$E2$ contributions are very small at this position because the FDMNES band structure calculations predict that the induced splitting is largly in the $5d$ and not the $4f$ band.

At this stage, it is not possible to make a definitive conclusion regarding the observation of an anapolar contribution to the XRS in multiferroic $TbMnO_3$. For one thing, the agreement between the data and the calculations based on the FDMNES code is only qualitative. While the code does a good job of accounting for the azimuthal dependences (Fig. 20) and spectra [Figs. 14, 19(g), and 19(h)], it overestimates the relative intensity of the (σ-σ') by a factor of roughly 5. However, it is probably reasonable to assert that, given the complex nature of the calculations, the agreement is about as good as might be achievable.

We reiterate here that the FDMNES calculations predicting an anapolar contribution at the C-type reflections assume a *Pbnm* space group. For this structure, the Tb ions lack a center of inversion and even in the absence of any ferroelectric order, an anapole moment on the Tb sites is allowed by symmetry. In the FDMNES calculations, the anapole contribution presumably is induced by the noncollinearity of the Mn moments in the cycloidal phase. Whether additional mechanisims contribute to the possible anapole moment, such as small shifts of the Tb positions, remains an open question.

Another explanation for the discrepancy between the calculated and experimental polarization dependence at the C-type reflections could be that, as we have already evoked for the A and F reflections observed at the Tb edge in the collinear phase, the C-type peaks might also have a charge multipole contribution in the cycloid phase. This could have the effect of increasing our measured $E1$-$E1$ XRS and thus making the experimental polarization ratio larger than the calculated one. In this respect, we are unable to draw a definitive conclusion. We also note a further weakness with the analysis. At present, the FDMNES code can only deal with one magnetic ion at a time. In addition to the cycloidal magnetic order on the Mn sublattice, the model of Kenzelmann *et al.*[17] has 1.0 μ_B on the Tb sublattice polarized along the **a** axis. Including just this latter component in the FDMNES code revealed unsurprisingly that at $(0,k\pm q,0)$, k odd, the $E2$-$E2$ contribution is larger than the one from $E1$-$E2$. However, this also introduced significant intensity at $(0,4\pm q,0)$ with an incorrect azimuthal dependence and we therefore consider it to be less consistent with our experimental data.

V. SUMMARY

We have carried out a comprehensive series of x-ray scattering experiments on multiferroic $TbMnO_3$ using both nonresonant and resonant techniques. In conceiving of the experiments, our hope was to be able to exploit the exquisite (and unique) ability of XRS to reveal and differentiate between possible multipolar order parameters. In particular, the transition from the collinear to the cycloidal and ferroelectric state in $TbMnO_3$, with the concomitant loss of inversion symmetry, should, at some level of sensitivity, be reflected by new features appearing below the transition arising from mixed $E1$-$E2$ processes. Evidence for such changes have in-

deed been found at both the Mn K (Fig. 13) and Tb L (Fig. 14) edges. However, the job of relating these observed changes to a microscopic description of the active multipoles is a considerable challenge and one that we have only gone part way to completing here. Our hope is that our data will serve to stimulate further theory and experiments in this class of materials.

More specifically, aided by NRXMS, which allowed us to characterize the magnetic domain structure within the sample volume probed by the x-ray beam, our experiments appear to have uncovered two previously unknown order parameters in this material. The NRXMS investigation has determined unambigously that our sample has a single A-type magnetic domain only. Nethertheless, XRS scattering is identified at F-type and C-type wave vectors, neither of which can be reconciled with XRMS from the nominal Mn magnetic order. Since the NRXMS results appear to exclude the $E1$-$E1$ F-type XRS observed at the Mn K edge from being magnetic in origin, we propose that it most likely arises from an induced charge multipole order parameter. If this is correct, then of crucial importance are the charge order satellites observed at $2q_{\mathrm{Mn}}$ about these F-type satellites, which suggest an intricate magnetic and charge order coupling in the material. We have attempted to further analyze the XRS results by implementing the FDMNES code, with varying degrees of success. Perhaps the most noteworthy outcome of these calculations is the identification of significant $E1$-$E2$ events in the Tb L_3 preedge of the XRS at C-type wave vectors in the magnetic cycloidal phase. Although our results at this stage should be considered as indicative only, our experiments may provide evidence for the existence of a novel type of anapolar order parameter in the rare-earth manganite class of multiferroic compounds.

Note added in proof. Recently, we realized that other XRS data has been recently reported with similar results on the induced polarization of the Tb ions at Mn magnetic wave-vectors.[39]

ACKNOWLEDGMENTS

We would like to thank S. Lovesey, K. Knight, C. Detlefs, M. Kenzelmann, P. Hatton, and A. Wills for helpful discussions. Work in Oxford was supported by the EPSRC and in London by a Wolfson Royal Society Research Merit Award and the EPSRC.

[1] T. Kimura, T. Goto, H. Shintani, K. Ishizaka, T. Arima, and Y. Tokura, Nature (London) **426**, 55 (2003).
[2] M. Fiebig, D. Frohlich, T. Lottermoser, and M. Maat, Phys. Rev. B **66**, 144102 (2002).
[3] T. Lottermoser, T. Lonkai, U. Amann, D. Hohlwein, J. Ihringer, and M. Fiebig, Nature (London) **430**, 541 (2004).
[4] T. Goto, T. Kimura, G. Lawes, A. P. Ramirez, and Y. Tokura, Phys. Rev. Lett. **92**, 257201 (2004).
[5] L. C. Chapon, G. R. Blake, M. J. Gutmann, S. Park, N. Hur, P. G. Radaelli, and S. W. Cheong, Phys. Rev. Lett. **93**, 177402 (2004).
[6] N. Hur, S. Park, P. A. Sharma, J. S. Ahn, S. Guha, and S. W. Cheong, Nature (London) **429**, 392 (2004).
[7] P. Carra and T. Thole, Rev. Mod. Phys. **66**, 1509 (1994).
[8] V. M. Bubovik and V. V. Tugushev, Phys. Rep. **187**, 145 (1990).
[9] B. Z. Dovich, Sov. Phys. JETP **33**, 1531 (1957).
[10] J. Goulon, C. Goulon-Ginet, A. Rogalev, V. Gotte, C. Malgrange, C. Brouder, and C. R. Natoli, J. Chem. Phys. **108**, 6394 (1998).
[11] J. Goulon, A. Rogalev, C. Goulon-Ginet, G. Benayoun, L. Paolasini, C. Brouder, C. Malgrange, and P. A. Metcalf, Phys. Rev. Lett. **85**, 4385 (2000).
[12] P. Carra, A. Jerez, and I. Marri, Phys. Rev. B **67**, 045111 (2003).
[13] I. Marri and P. Carra, Phys. Rev. B **69**, 113101 (2004).
[14] S. Di Matteo, Y. Joly, and C. R. Natoli, Phys. Rev. B **72**, 144406 (2005).
[15] S. Di Matteo and Y. Joly, Phys. Rev. B **74**, 014403 (2006).
[16] S. W. Lovesey, E. Balcar, K. Night, and J. F. Rodriguez, Phys. Rep. **411**, 233 (2005).
[17] M. Kenzelmann, A. B. Harris, S. Jonas, C. Broholm, J. Schefer, S. B. Kim, C. L. Zhang, S. W. Cheong, O. P. Vajk, and J. W. Lynn, Phys. Rev. Lett. **95**, 087206 (2005).
[18] R. Kajimoto, H. Yoshizawa, H. Shintani, T. Kimura, and Y. Tokura, Phys. Rev. B **70**, 012401 (2004).
[19] Y. Yamasaki, S. Miyasaka, Y. Kenako, J. P. He, T. Arima, and Y. Tokura, Phys. Rev. Lett. **96**, 207204 (2006).
[20] G. Lawes, A. B. Harris, T. Kimura, N. Ragado, R. J. Cava, A. Aharony, O. Entin-Wohlman, T. Yildrim, M. Kenzelmann, C. Broholm, and A. P. Ramirez, Phys. Rev. Lett. **95**, 087205 (2005).
[21] A. B. Harris, T. Yildirim, A. Aharony, and O. Entin-Wohlman, Phys. Rev. B **73**, 184433 (2006).
[22] H. Katsura, N. Nagaosa, and A. V. Balatsky, Phys. Rev. Lett. **95**, 057205 (2005).
[23] E. O. Wollan and W. C. Koehler, Phys. Rev. **100**, 545 (1955).
[24] E. F. Bertaut, Acta Crystallogr., Sect. A: Found. Crystallogr. **A84**, 217 (1968).
[25] S. Quezel, F. Tcheou, J. Rossatmighod, G. Quezel, and E. Roudaut, Physica B & C **86**, 916 (1977).
[26] J. Blasco, C. Ritter, J. Garcia, J. M. de Teresa, J. Perez-Cacho, and M. R. Ibarra, Phys. Rev. B **62**, 5609 (2000).
[27] T. Arima, T. Goto, Y. Yamasaki, S. Miyasaka, K. Ishii, M. Tsubota, T. Inami, Y. Murakami, and Y. Tokura, Phys. Rev. B **72**, 100102(R) (2005).
[28] N. Aliouane, D. N. Argyriou, J. Strempfer, I. Zegkinoglou, S. Landsgesell, and M. v. Zimmermann, Phys. Rev. B **73**, 020102(R) (2006).
[29] Y. Joly, Phys. Rev. B **63**, 125120 (2001).
[30] T. Kimura, S. Ishihara, H. Shintani, T. Arima, K. T. Takahashi, K. Ishizka, and Y. Tokura, Phys. Rev. B **68**, 060403(R) (2003).
[31] J. Paolasini, C.Detlefs, C. Mazzoli, S. Wilkins, P. Deen, A. Bomberdi, N. Kernavanois, F. de Bergevin, F. Yakhou, J. P. Valade, I. Breslavetz, A. Fondacaro, G. Pepellin, and P. Benard, J. Synchrotron Radiat. **14**, 301 (2007).
[32] K. D. Finkelstein, Q. Shen, and S. Shastri, Phys. Rev. Lett. **69**, 1612 (1992).

[33] D. H. Templeton and L. K. Templeton, Acta Crystallogr., Sect. A: Cryst. Phys., Diffr., Theor. Gen. Crystallogr. **38**, 62 (1982).
[34] Y. Murakami, J. P. Hill, D. Gibbs, M. Blume, I. Koyama, M. Tanaka, H. Kawata, T. Arima, Y. Tokura, K. Hirota, and Y. Endoh, Phys. Rev. Lett. **81**, 582 (1998).
[35] R. Kajimoto, H. Mochizuki, H. Yoshizawa, H. Shintani, T. Kimura, and Y. Tokura, J. Phys. Soc. Jpn. **74**, 2430 (2005).
[36] M. Blume and D. Gibbs, Phys. Rev. B **37**, 1779 (1988).
[37] J. P. Hill and D. F. McMorrow, Acta Crystallogr., Sect. A: Found. Crystallogr. **52**, 236 (1996).
[38] D. Mannix, A. Stunault, N. Bernhoeft, L. Paolasini, G. H. Lander, C. Vettier, F. de Bergevin, D. Kaczorowski, and A. Czopnik, Phys. Rev. Lett. **86**, 4128 (2001).
[39] J. Voigt, J. Persson, J. W. Kim, G. Bihlmayer, and Th. Brückel, Phys. Rev. B **76**, 104431 (2007).